

Takahisa Shiratori · Yuji Tasaka · Yuichi Murai ·
Yasushi Takeda

Development of ultrasonic visualizer for capturing the characteristics of viscoelastic fluids

Received: 18 April 2013 / Revised: 22 June 2013 / Accepted: 29 July 2013 / Published online: 7 September 2013
© The Visualization Society of Japan 2013

Abstract In the field of rheology, properties of non-Newtonian fluids have been traditionally represented on graphs such as viscosity curves. In this paper, we propose a visualizer to express the fluid properties as visualized fluid motions in a rotating cylinder. To highlight different fluid motions, three patterns of rotation were given to the cylinder: rapid start of constant rotation (spin-up), rapid stop from constant rotation (spin-down), and periodic rotation. Relationships between fluid motion and fluid properties are discussed by comparing velocity profiles for three fluids: silicone oil, yogurt, and a polyacrylamide (PAA) solution. Ultrasonic velocity profiler (UVP) was used to obtain spatio-temporal velocity maps. The velocity maps reflect essential rheological properties, such as shear thinning, yield stress, and elasticity. Two additional display modes are proposed to explore fluid motions due to viscoelasticity of the PAA solution and yogurt: a grid deformation field and a shear rate field. These two visualizations can provide intuitive understanding of viscoelasticity because deformation and shear rate determine elastic and viscous stresses, respectively. In spin-down tests, the recovery of deformed grids, which is caused by elasticity, can be explicitly observed. Further, the shear rate distributions indicate that kinetic energy of the fluid dissipates near the lateral wall right after the wall stops rotating. In short, these two quantity fields visualize energy conversion among kinetic, elastic, and thermal energy; such energy conversions are characteristic of viscoelastic fluids.

Keywords Ultrasonic velocity profiler (UVP) · Property visualization · Viscoelasticity · Shear thinning · Rheology

1 Introduction

Flow visualization has long been recognized as a way to capture fluid motion, for example leaves floating on rivers, snow swirling around buildings, and minced vegetables floating on soup. Flow visualization has been sophisticated as an important tool in experimental fluid mechanics, and over the last decades, it has evolved into a quantitative tool, namely particle imaging velocimetry (PIV). Various techniques for flow visualizations of Newtonian fluids, such as water and air, have been described in many published text books. However, in the field of rheology, complex behaviors on flows of non-Newtonian and viscoelastic fluids, such as milk and paint, are often invisible because of opaqueness. Therefore, approaches using flow

T. Shiratori (✉) · Y. Tasaka · Y. Murai
Graduate School of Engineering, Hokkaido University, N13 W8,
Sapporo 060-8628, Japan
E-mail: t.shiratori@ring-me.eng.hokudai.ac.jp
Tel.: +81-11-7066373
Fax: +81-11-7066373

Y. Takeda
Institute of Food, Nutrition and Health, ETH Zurich, Schmelzbergstrasse 7, 8092 Zurich, Switzerland

visualization have been inhibited and less popular to date. Rheologists focus on measurement of rheological properties in various substances and numerically visualize entire flow structures with CFD to understand the influence of the properties. Experimental flow visualization is always desirable to validate the effective range and universality of rheological properties and models. In the point of view of the fluid mechanics, flow fields reflect all physical properties of fluids and the physical effects acting in a fluid. Therefore, the experimental visualizations of velocity and strain field, which represent momentum transfer and material deformation, should be able to provide intuitive images that capture the flow characteristics of rheological fluids.

Some visualization techniques are applicable to opaque fluids, such as ultrasonic velocity profiling (UVP) (Wiklund et al. 2006; Murai et al. 2010; Yanagisawa et al. 2010; Takeda 2012), ultrasonic echo image processing (Zheng et al. 2006), X-rays (Lee et al. 2009; Bauer et al. 2012), neutron radiography (Geiger et al. 2002) and NMRI (Sinton et al. 1994). Except for ultrasonic applications, these techniques require special facilities and licenses and, therefore, their use is available only to a very few researchers. In contrast, ultrasonic techniques are widely available than other techniques and are radiation free. In particular, UVP can be easily implemented: basically, all that is required is attaching an ultrasonic transducer to a wall of flow facilities. In addition, because of its fast-signal analysis, UVP is capable of monitoring instantaneous velocity profiles such as flow field visualization. To date, UVP has a wide range of application fields, as summarized in the book by Takeda 2012. Because of its wide applicability, UVP has already been applied to characterization of non-Newtonian fluids (Ouriev and Windhab 2002; Birkhofer et al. 2008; Kotze et al. 2012). The measurable property is still limited to shear-rate-dependent viscosity under steady flows, but this work suggests future potential uses of UVP in rheology.

In this paper, we propose a UVP-based visualizer for capturing the characteristics of viscoelastic fluid motions. Flow fields contain rich information about fluid properties and fluid mechanics. Therefore, the present flow visualizer provides information that is familiar to general researchers and intuitive images about flow characteristics of rheological fluids, rather than just specific values for rheological properties, which has commonly been done in rheology. Further, with the help of knowledge about rheology, this visualizer would be an effective tool for estimating rheological properties at industrial sites, like interpretations of radiograms at the medical front.

As the first step in system development, we have devoted most of our efforts to investigating viscoelastic fluids. Because flow behaviors of viscoelastic fluids change depending on the flow system, selection of the system determines the success of development. We adopt rotating flows in a cylinder as the flow system, because such a system achieves simple one-dimensional flows and allows wide variations in rotation. The viscoelastic nature of fluids is emphasized in unsteady flows. Thus, we employ three different rotation tests: (a) sudden starts from a stationary state (spin-up), (b) sudden stops from steady-state rotation (spin-down), and (c) periodic oscillations. To highlight the viscoelastic behavior of the fluid, we developed three ways of visualization: (1) direct flow field visualization in the cylinder, (2) strain field visualization, and (3) shear rate field visualization. On the results of visualizations for three test fluids (a viscous silicone oil, a polyacrylamide (PAA) solution, and yogurt), we explain how to capture viscoelastic characteristics.

2 Experimental apparatus and conditions

To observe the viscoelastic motions of fluids, we used a cylindrical container having a height of 300 mm and an inside diameter of 154 mm. A schematic top view of the container is shown in Fig. 1. A stepping motor was connected to the bottom to rotate the whole cylinder. The container was filled with a test fluid and covered by a lid. An ultrasonic transducer for UVP with 2 MHz in the basic frequency was installed at the position indicated in Fig. 1, 150 mm from the bottom and $d = 7$ mm horizontally from the center line. This horizontal displacement from the center line makes it possible to obtain the radial profiles of the azimuthal velocity component. The cylindrical container and ultrasonic transducer were settled in a rectangular container filled with water to improve the transmission rate of ultrasonic waves and to prevent multiple reflections of ultrasonic waves from cylindrical walls. As UVP device, a commercial system, UVP-DUO (Met-Flow, S.A.) was adopted for signal processing. Each measurement volume has a thin disk shape with 0.98 mm in thickness. The diameter of the measurement volume changes depending on the position because of divergence of the ultrasonic beam, and ranges from 10 to 20 mm. There is a near-field region, where the ultrasonic beam is unstable, from the front of the transducer to 33.8 mm, and we omit the velocity information obtained at the corresponding positions.

Placing the measurement line off the center line of the cylinder (d in Fig. 1) enables us to obtain the azimuthal velocity component. Velocities measured on the line contain both radial velocity component, u_r , and tangential velocity component, u_θ . Assuming the axial symmetry of the flows, these velocity components can be extracted from the following formulae:

$$u_\theta = \frac{u_{\xi, \text{far}} + u_{\xi, \text{near}}}{2 \cos \alpha}, \quad (1)$$

$$u_r = \frac{u_{\xi, \text{far}} - u_{\xi, \text{near}}}{2 \sin \alpha}, \quad (2)$$

where $u_{\xi, \text{far}}$ and $u_{\xi, \text{near}}$ represent the velocities measured at the far side and the near side halves of the cylinder by UVP and α is the angular coordinate of the measurement point against the center of the cylinder, as shown in Fig. 1.

Three test fluids were used in the experiments: silicone oil (Shin-Etsu Chemical, KF96-1000cs), 0.5 wt% polyacrylamide (PAA) solution (Dia-Nitrix, AP825C), and yogurt (Meiji, LB81 plain). Silicone oil is regarded as a Newtonian fluid with a viscosity of 0.97 Pa s. The PAA solution has shear-rate-dependent viscosity and viscoelasticity. Figure 2a, b shows the viscosity curve and dynamic moduli, storage modulus G' and loss modulus G'' , measured with a rotational rheometer MCR301 (Anton Paar). As Fig. 2a indicates, PAA solution is shear thinning fluid whose viscosity obeys the power law. At the same time, PAA solution has viscoelasticity. According to Fig. 2b, storage modulus G' always exceeds loss modulus G'' in the measurable frequency range. The yogurt is an example of an opaque and viscoelastic fluid with uncertain rheological properties. In silicone oil and PAA solution, resin powders, FLO-BEADS CL-2507 (Sumitomo

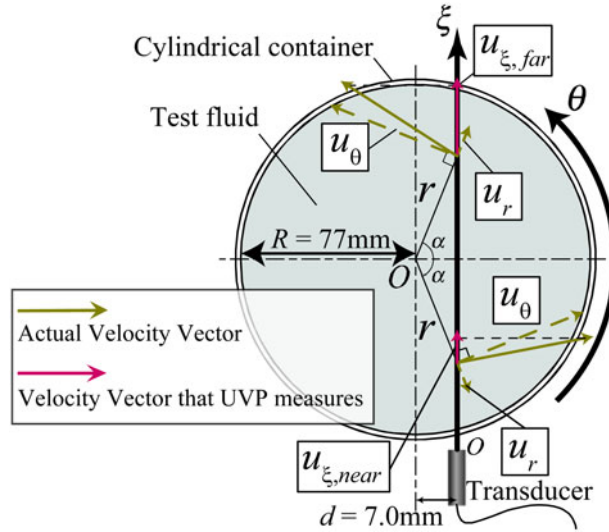


Fig. 1 Experimental apparatus

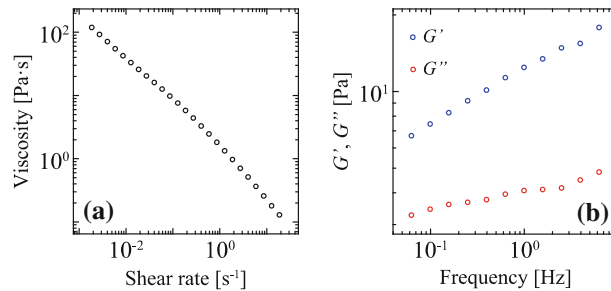


Fig. 2 **a** Shear-rate-dependent viscosity and **b** storage and loss moduli of 0.5 wt% PAA solution measured with rotational rheometer

Seika Chemicals), and DIAION HP20SS (Mitsubishi Chemical) were dispersed, respectively, as ultrasound reflectors. In the yogurt, the fat content reflects ultrasonic waves (Wiklund and Standing 2008, Wiklund et al. 2010), so seeding particles were not needed.

To observe unsteady flows, three patterns of rotation were given to the cylindrical container: rapid start of constant rotation (spin-up), rapid stop from constant rotation (spin-down), and periodic oscillations. In spin-up tests, the container suddenly accelerated at $t = 0$ to the lateral wall speed $U_{\text{wall}} = 101$ mm/s (the corresponding rotation rate was 12.5 rpm). After that, the rotation was suddenly stopped at $t = 5.0$ s (spin-down test). The duration time of rotation was long enough for fluids to reach rigid-body rotation. In the oscillation tests, oscillatory rotation was applied to the container from the initial stationary condition. Time variations of the velocity on the lateral wall are described by

$$U_{\text{osc}} = U_0 \sin 2\pi ft, \quad (3)$$

where U_0 is the amplitude of velocity (760 mm/s) and f is the frequency of oscillation (0.5 Hz).

3 Fluid properties indicated by velocity profiles

For each of the three test fluids, Fig. 3 shows the profiles of the tangential velocity component u_θ calculated from Eq. (1) for the three tests: spin-up, spin-down, and oscillation. In all velocity maps, the radial coordinate has been normalized by the radius of the cylindrical container $R = 77$ mm. In the spin-up and spin-down tests, the color code for velocity was set to drastically change at $u_\theta = 0$; this emphasizes the appearance of negative velocities that appear as the result of fluid elasticity. We can observe deep-purple stripes before the rotation when the fluid should be stationary, but their magnitudes correspond to several fold of velocity resolution. So, we assume that these are noise due to the measurement characteristics for stationary fluid. In the spin-up and spin-down tests, the velocities were normalized by the velocity of the lateral wall ($U_{\text{wall}} = 101$ mm/s); in oscillation tests, they were normalized by the amplitude of the wall velocity ($U_0 = 760$ mm/s). Velocities near the wall ($r/R > 0.9$) could not be captured, because the ultrasound beam could not be focused enough. Multi-reflection of the ultrasound beam in the cylindrical wall also prevents velocity profiling.

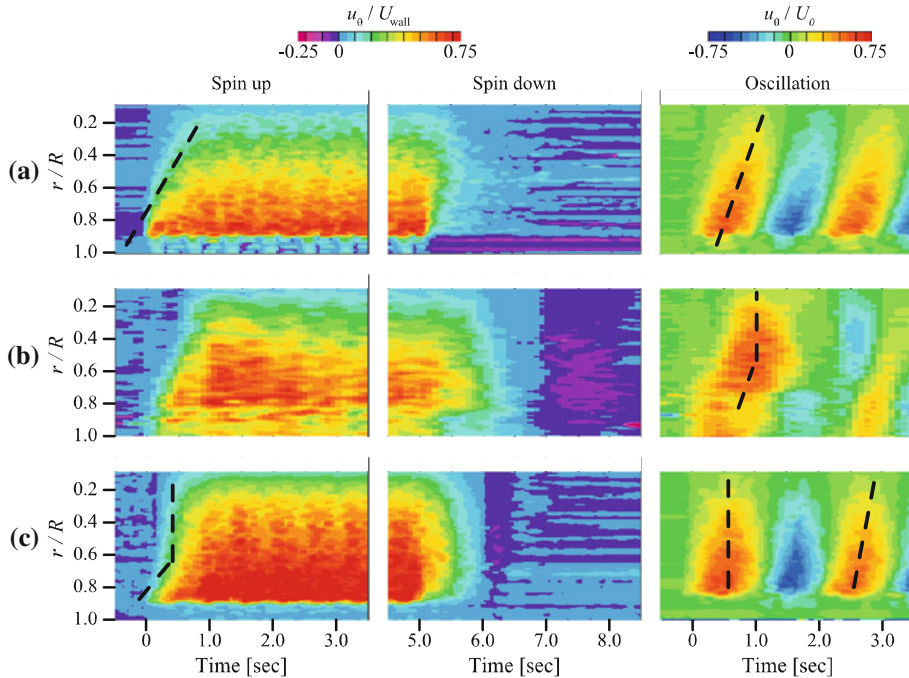


Fig. 3 Velocity profiles of **a** silicone oil, **b** PAA solution, and **c** yogurt under three rotational conditions (spin-up, spin-down, and oscillation)

In spin-up tests shown in the left panels of Fig. 3, the cylinder begins to rotate at $t = 0$. At first, the lateral wall, which has the non-slip condition against the fluid, induces azimuthal motion of fluid near the wall. Then, azimuthal momentum transferred from the wall to the fluid propagates to the core fluid region by viscous diffusion. After that, the fluid motion reaches rigid-body rotation, which is the terminal condition of spin-up tests. Momentum propagation appears as a contour line in velocity profiles as a dotted line in the left panel of Fig. 3a. The angle between the contour line and the horizontal axis represents the speed of momentum propagation, which is determined by the viscosity of the test fluid: larger angles indicate larger viscosities. For yogurt, the left panel in Fig. 3c shows that the speed of propagation depends on the radial position. Near the wall, $r/R > 0.7$; it takes time for the momentum to propagate. But in the core region of the fluid, the contour lines are almost vertical. This means that the yogurt in the core region remains in a rigid-body state even while accelerating. This observed behavior is consistent with the fact that yogurt has yield stress as it changes from a solid-like state to fluid. Near the wall, the shear stress exceeds the yield stress because of the strong shear, and the yogurt behaves like a fluid. However, in the core region, the shear stress is less than the yield stress, and the yogurt behaves like a solid.

In the spin-down tests, the cylinder stopped rotating at $t = 5.0$ s. Until just before the stop, fluids rotated rigidly, but after the cylinder stopped, test fluids were decelerated by the lateral wall. Elastic behavior was most clearly observed in spin-down tests. Reverse flows were observed at $t > 7.0$ s for the PAA solution and at $6.0 < t < 6.5$ s for the yogurt. These reverse flows must be caused by elasticity because the lateral wall does not introduce any momentum in the negative direction. Moreover, reverse flows were not observed in silicone oil, which is regarded as an inelastic fluid. Velocity profiles during deceleration in spin-down tests indicate that kinetic energy is stored as elastic energy in viscoelastic fluids, and the fluid is driven in the negative direction when that elastic energy is reconverted to kinetic energy.

In the oscillation tests, oscillatory motion was applied to the cylinder in accordance with Eq. (3) starting at $t = 0$. The right panel of Fig. 3a shows that the velocity profile for silicone oil displays sinusoidal oscillations at each position. The frequency of the velocity fluctuations is almost the same as that of the lateral wall ($f = 0.5$ Hz). This means that there are no non-linear interactions during momentum propagation in the oil. The amplitude of the velocity is large near the lateral wall. However, silicone oil in the core region has a phase lag relative to the lateral wall, as indicated by the dotted line in the right panel of Fig. 3a. This phase lag depends on the viscosity: the dotted line would tilt to the horizontal axis if the viscosity of the fluid is small, but it would tilt to the vertical axis if the viscosity is large. For the PAA solution, the time variations in velocity deviate from a simple sinusoidal curve. This is because of viscoelasticity. After a sufficiently long time, the time variations in velocity converge to a sinusoidal curve. On the basis of the phase lag, the viscosity of the PAA solution is small near the lateral wall and large near the center, as the dotted line in Fig. 3b indicates. This spatial variation of the viscosity is consistent with shear thinning of the PAA solution; in shear thinning fluids, the viscosity decreases as the shear acting on the fluid increases. For yogurt, the time variations in velocity are almost sinusoidal. The differences between the velocity profiles of the yogurt and silicone oil are the phase lags at different positions. In yogurt, the phase lag is small, especially during the initial cycle because the yogurt remains in a rigid-body state during the initial cycle of the oscillation. In the second cycle, the dotted line tilts more horizontally than in the initial cycle. This behavior suggests a decrease in viscosity. The stress acting on the yogurt exceeds the yield stress in the oscillation; therefore, the viscosity changes from infinity (i.e., a solid state) to a finite value after yielding.

4 Vector expressions of velocity for intuitive understanding

Spatio-temporal velocity maps, such as those in Fig. 3, contain full information about flow characteristics and fluid properties. However, those maps do not provide direct images of fluid motions in real physical coordinates. The displays of velocity vector profiles are a better way of visualization for intuitive understanding. Figures 4, 5, and 6 show velocity vector fields at select times during the spin-down of the silicon oil, PAA solution, and yogurt, respectively. The corresponding spatio-temporal velocity distributions are shown in the center panel of Fig. 3. As described by Eq. (1) and (2), both tangential and radial velocity components, u_θ and u_r , can be derived from spatio-temporal velocity profiles provided by UVP. Both velocity components are displayed as the vector fields in Figs. 4, 5, and 6. Those figures show that the radial component u_r is negligible compared to the tangential component u_θ . Hence, only u_θ is taken into account in the two visualization modes described in the following sections.

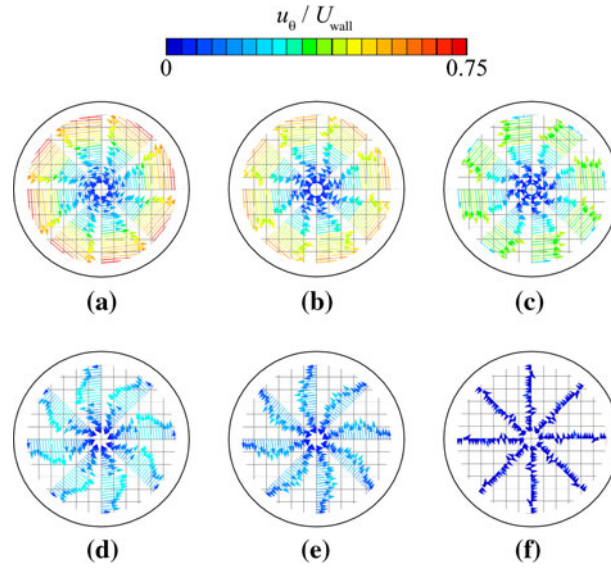


Fig. 4 Velocity vector fields of silicone oil in the spin-down process at these times: $t =$ **a** 5.00 s, **b** 5.06 s, **c** 5.12 s, **d** 5.23 s, **e** 5.35 s, and **f** 6.34 s

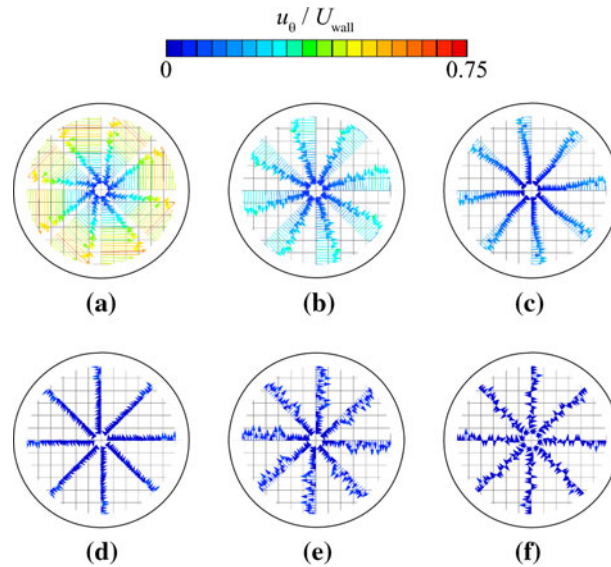


Fig. 5 Velocity vector fields of the PAA solution in the spin-down process at these times: $t =$ **a** 5.00 s, **b** 5.98 s, **c** 6.25 s, **d** 6.60 s, **e** 7.40 s, and **f** 8.56 s

For the spin-down tests, Figs. 4a, 5a, and 6a indicate velocity vector fields at $t = 5.0$ s, at which the rotation of the cylinder is just stopped after the flow reaches the rigid-body rotation. The linear trend in vector length vs. radial position indicates that all three fluids remain in rigid-body rotation at the time. After that, the fluids are decelerated by the lateral wall. Figure 4c, d, e provides clear images of the deceleration process in silicone oil: velocities are small near the wall, and a maximum velocity occurs near $r/R = 0.5$. After deceleration, the velocities reach zero all along the radial positions, as shown in Fig. 4f. The PAA solution follows a deceleration process that is similar to that of silicone oil until the velocities first become zero at Fig. 5d, but then, unlike silicone oil, reverse flows due to elasticity appear as shown in Fig. 5e. After that the PAA solution displays oscillations around zero velocity with decreasing amplitudes until finally the flow reaches a stationary state, as shown in Fig. 5f. Unfortunately, cycles in oscillations after the initial one cannot be distinguished on the velocity vector profile, because their small velocities were buried in measurement noise. For the yogurt, deceleration was similar to that of the PAA solution: velocities first become

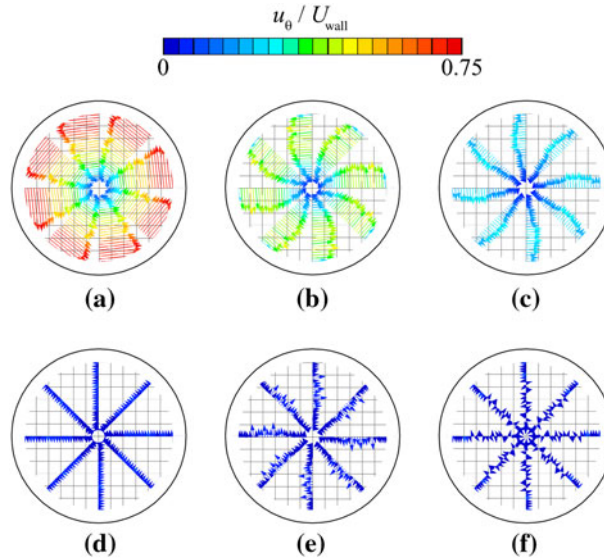


Fig. 6 Velocity vector fields of yogurt in the spin-down process at these times: $t =$ **a** 5.00 s, **b** 5.23 s, **c** 5.49 s, **d** 5.88 s, **e** 6.14 s, and **f** 6.56 s

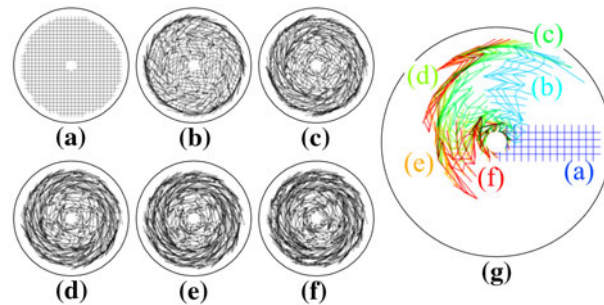


Fig. 7 Deformation of grid pattern for silicone oil in the spin-down process at these times: $t =$ **a** 5.00 s, **b** 5.23 s, **c** 5.46 s, **d** 5.70 s, **e** 5.93 s, and **f** 6.13 s. Parts of the grids are superposed in (g)

zero in Fig. 6d and then reverse flows appear in Fig. 6e. However, the duration of reverse flow of the yogurt was shorter than that of the PAA solution, suggesting that yogurt has larger elasticity than the PAA solution.

The reverse flows of the PAA solution and yogurt were due to elastic energy stored in those viscoelastic fluids. If the test fluid is a perfect elastic body, the stored elastic energy is proportional to the square of the strain. It is possible to imagine how much and where the elastic energy is stored by watching the strain fields. In the next section, deformations of a grid pattern, which represents fluid deformations, are calculated from the velocity profiles in Fig. 3. Those deformations provide semi-quantitative visualizations of the strain and help us grasp the elastic energy distribution.

5 Visualization of stored elastic energy

Because elastic stress and stored elastic energy are determined by strain, visualizing the strain field has great importance in the discussion of viscoelasticity. In spin-down tests, reverse flows, caused by stored elastic energy, were observed. Therefore, we visualized the strain field during spin-down tests by calculating how grid patterns are deformed by fluid motion. The calculated deformations are shown in Figs. 7, 8, and 9, for silicone oil, PAA solution, and yogurt, respectively. The initial conditions were defined by the undeformed grids shown in (a) of each figure at $t = 5.0$ s. From this initial condition, cross points are moved according to the velocity profile shown in Fig. 3: tangential positions of cross points $\theta(t)$ are determined by

$$\theta(t) = \int_{t_{\text{stop}}}^t \frac{u_{\theta}(t')}{r} dt', \quad (4)$$

where t_{stop} means time when the rotation of the cylinder is stopped: $t = 5.0$ s. The moved points are connected by straight lines. At the initial condition, the test fluids were rigidly rotating without any stress. Thus, the calculated deformations represent deviations from the initial stress-free state. Under this expression, viscous characteristics appear as the deformation remaining at the terminal state, whereas elastic characteristics appear as the recovery from the deformed state. Time variations in the deformations are shown in the image sequence from (a) to (f) in Figs. 7, 8, and 9. Parts of each sequence are superposed in (g), where grid patterns at each time step are displayed with a different color.

Even after the wall is stopped, fluids move in the tangential direction because of inertia. This produces a velocity gradient against the stationary cylinder wall and thus the fluids near the wall are deformed, as shown in Fig. 7b. Then the inner fluid is deformed while being stopped. Thus, silicone oil is deformed at all radial positions when the fluid is completely stopped, as shown in Fig. 7f. If a perfect elastic body experiences this same deformation, the fluid moves in the negative direction and continues to oscillate forever. However, silicone oil does not exhibit any reverse flow, as shown in Fig. 3a. This indicates that silicone oil does not have elasticity, and all the initial kinetic energy in Fig. 7a is converted to thermal energy. In the stationary condition, shown in Fig. 7f, all the kinetic energy has been converted to thermal energy.

In contrast, the deceleration processes of the PAA solution and yogurt are not monotonic. For example, for the PAA solution, the fluid near the wall is deformed at first, as shown in Fig. 8b. Then, the velocity first becomes zero at all radial positions in Fig. 8e. The reverse flow induced by the release of elastic energy occurs at a time between Fig. 8e and f. The strain in Fig. 8e partially recovers and finally converges to the stationary terminal state, as in Fig. 5f. The reverse flow and the recovery of the deformation can be clearly seen in Fig. 8g as the variation from (e) to (f). The yogurt undergoes deceleration similar to the PAA solution: the yogurt is first deformed near the wall (Fig. 9b), then stops the first time (Fig. 9e), and recovers slightly (from Fig. 9e, f). The magnitudes of the relaxations in deformations from (e) to (f) in Figs. 8 and 9 should be a measure of the degree of elasticity, because the distance is determined by the stored elastic energy. According to this, the PAA solution is more elastic than the yogurt.

As already mentioned, a perfectly elastic fluid should oscillate forever in spin-down tests. However, in the present experiments, the fluids lose kinetic energy and reach a stationary state while maintaining the deformation. This means that a large part of the initial kinetic energy is not stored as elastic energy, but dissipated as thermal energy. One factor that determines the amount of energy dissipation is the shear rate. Thus, to estimate the magnitude of viscous energy dissipation, the shear rate distribution is visualized in the next section.

6 Visualization of viscous energy dissipation

In Sect. 5, we visualized the strain distribution, which is related to stored elastic energy. On the other hand, viscosity causes the energy dissipation that occurs in high-amplitude shear rate regions. Therefore, to understand how viscosity contributes to the motion of fluids, we now visualize the shear rate distribution in spin-down tests. Figures 10, 11, and 12 present images of the shear rate distribution. In those figures, the colors indicate the local shear rate, which was calculated by

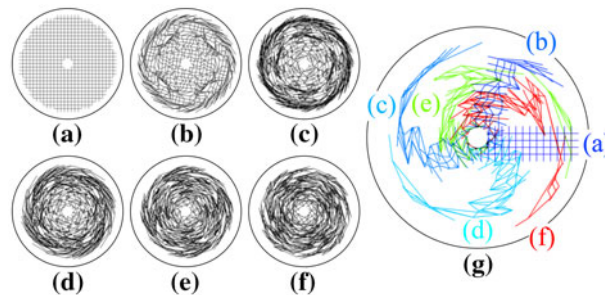


Fig. 8 Deformation of grid pattern for the PAA solution in the spin-down process at these times: $t =$ **a** 5.00 s, **b** 5.18 s, **c** 5.45 s, **d** 5.71 s, **e** 7.14 s, and **f** 8.56 s. Parts of the grids are superposed in **(g)**

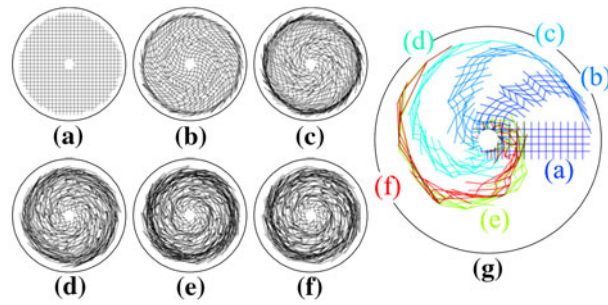


Fig. 9 Deformation of grid pattern for yogurt in the spin-down process at these times: $t =$ **a** 5.00 s, **b** 5.10 s, **c** 5.23 s, **d** 5.44 s, **e** 6.01 s, and **f** 6.59 s. Parts of the grids are superposed in (**g**)

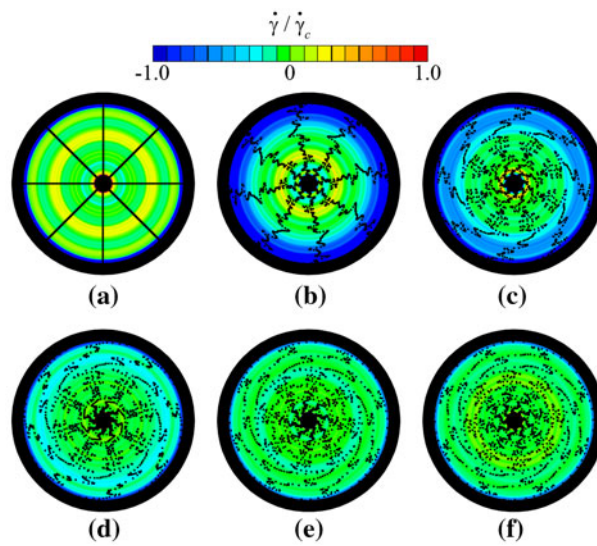


Fig. 10 Particle motions (*black dots*) and shear rates (*colors*) for silicone oil flows at $t =$ **a** 5.00 s, **b** 5.15 s, **c** 5.32 s, **d** 5.49 s, **e** 5.67 s, and **f** 5.84 s

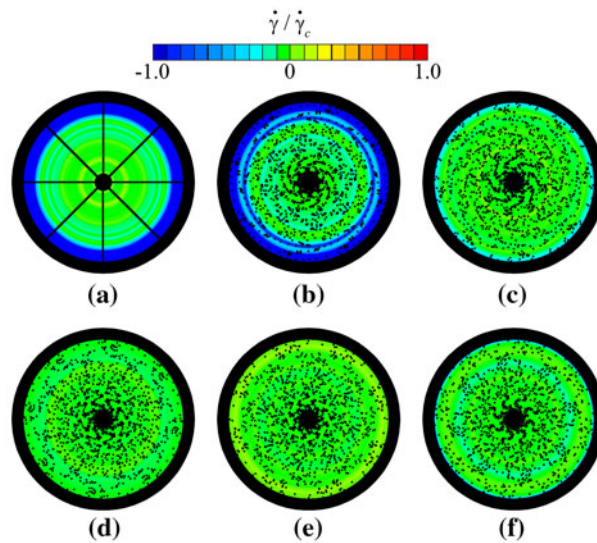


Fig. 11 Particle motions (*black dots*) and shear rates (*colors*) for PAA solution flows at $t =$ **a** 5.00 s, **b** 5.62 s, **c** 6.34 s, **d** 7.05 s, **e** 7.76 s, and **f** 8.47 s

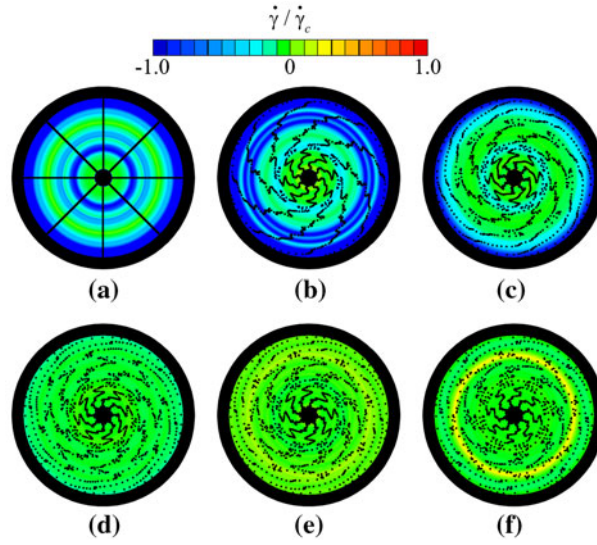


Fig. 12 Particle motions (*black dots*) and shear rates (*colors*) of yogurt flows at $t =$ **a** 5.00 s, **b** 5.29 s, **c** 5.60 s, **d** 5.91 s, **e** 6.22 s, and **f** 6.53 s

$$\dot{\gamma} = \frac{\partial u_{\theta}}{\partial r} - \frac{u_{\theta}}{r}. \quad (5)$$

Shear rates were normalized by the characteristic shear rate, which is defined by

$$\dot{\gamma}_c = \frac{U_{\text{wall}}}{R}. \quad (6)$$

As shown in Eq. (5), the calculation requires the differential of the experimental velocity. Often, such differentials are numerically estimated using a simple finite difference. However, in this case a finite difference enhances noise in the measurements. To avoid amplifying the noise, least square fitting was applied to the data: velocity gradient in Eq. (5) was calculated by

$$\left(\frac{\partial u_{\theta}}{\partial r} \right)_i = \frac{(2n+1) \sum_{j=i-n}^{i+n} r_j u_{\theta j} - \sum_{j=i-n}^{i+n} r_j \sum_{j=i-n}^{i+n} u_{\theta j}}{(2n+1) \sum_{j=i-n}^{i+n} r_j^2 - \left(\sum_{j=i-n}^{i+n} r_j \right)^2}, \quad (7)$$

where $2n + 1$ corresponds to the spatial range for the fitting. In the figures, n was set as 20. This indicates that structures smaller than 10 mm cannot be resolved in the figures. This spatial range is smaller than the energy dissipating area, yet large enough to reduce local noise caused by finite difference calculation. The strain acting on the fluid is also displayed as particle motions determined by Eq. (4). At the initial position, the particles align in the radial direction at $t = 5.00$ s, as shown in (a) of Figs. 10, 11, and 12. Therefore, both viscous and elastic contributions to the stress are visualized in the same figures.

After the lateral wall was stopped, the fluid near the wall also stopped. However, the fluid far from the wall remained in motion because of inertia. This situation produced negative shear rates, as shown by the blue areas near the lateral walls in Figs. 10b, c, 11b, and 12b. In these areas, kinetic energy is dissipated as thermal energy. The energy conversion during reverse flow is easily seen in Fig. 12 for yogurt. After deceleration caused by the lateral wall, velocities become zero everywhere. Then the shear rate also becomes zero, of course, as shown in Fig. 12d. However, the fluid still has energy as elastic energy, as shown by the deformed distribution of particles in Fig. 12d. Thus, the reverse flow and corresponding positive shear rates appear in Fig. 12e, f as yellow rings a little inside from the cylinder wall. Viscoelastic fluids such as yogurt should undergo repeated azimuthal oscillations around zero velocity with decreasing amplitudes, but those small velocities cannot be resolved on the velocity profiles shown here. Thus, the value of the shear rate also should oscillate around zero, and viscous dissipation occurs in the regions of both

positive and negative shear rates. While the oscillations continue, the amplitudes of shear rate and velocity decrease. In the terminal state, the shear rate and velocity become zero everywhere because all kinetic energy has been converted to thermal energy.

7 Conclusion

With the aim of obtaining intuitive images of characteristic flows induced by viscoelasticity, we developed an ultrasonic visualizer for the flows of viscoelastic fluids. The system consists of an ultrasonic velocity profiler (UVP) and a cylindrical container that can undergo various rotational modes. To highlight viscoelastic behavior, we applied three display modes (velocity vector profiles, fluid deformations, and shear rate distributions) to data taken from three rotational modes (spin-up, spin-down, and oscillation). For evaluating the applicability of the visualizer, three fluids were examined: two non-Newtonian fluids having different elasticities (a polyacrylamide (PAA) solution and yogurt) and, for comparison, an inelastic Newtonian fluid (silicone oil). The use of yogurt also emphasized the ability of the visualizer to provide images from opaque fluids, because most industrial viscoelastic fluids are opaque.

Before demonstrating the three display modes, we read out essential information about flow characteristics obtained from experimentally determined spatio-temporal velocity maps. Spin-up tests indicated differences in the relative viscosities of the three fluids, and variations of contours on the velocity maps implied yield stresses in the yogurt. Spin-down tests explicitly revealed elastic behavior in the form of reverse flows. These influences were superimposed in the oscillation tests. For capturing viscoelastic effects, the spin-down test is most suitable because of the clear appearance of reverse flows.

Therefore, we demonstrated the three display modes on the basis of the spin-down tests applied to each of the three fluids. The velocity vector profiles produce intuitive visual understanding of momentum propagation from the wall to the inner fluid and, thus, the users of the visualizer can directly extract magnitudes of relative viscosity and behavior of viscoelastic fluids. A grid pattern display can provide visualized information about fluid deformations that correspond to strain. Strain distributions provide information about the storage of elastic energy, deformations remaining at terminal stationary states, and mean energy dissipations to thermal energy caused by viscosity. Viscous dissipation and the storage of energy are simultaneously visualized in a display of both shear rate distribution and fluid particle motions representing deformation of the fluid. In these three display modes, we restricted the object of the visualizer to viscoelasticity for demonstration purposes in this paper. In fact, the visualizer has wider applicability than what is presented here; for example, it can be adopted for visual detection of complex rheological responses, such as yield stress, shear thinning, or thickening effects.

Flow fields reflect all physical properties of fluids and the physical effects acting on fluids. Therefore, spatio-temporal velocity maps, which contain quantitative information about flow fields, can provide viscoelastic properties of fluids as specific values. However, this cannot be done in the current configuration, because the determination of specific values requires information about stress at the boundaries. We are designing new equipment that consists of the present visualizer and a torque meter; this new device should satisfy the demands of providing intuitive visual images as well as explicit values for physical properties of viscoelastic fluids.

Acknowledgments We would like to express our thanks to Prof. H. Orihara in the Laboratory of Softmatter Physics, Hokkaido University, for providing the opportunity to use the rotational rheometer and measure rheological properties in Fig. 2. Polyacrylamide used in this study was proffered by Dia-Nitrix Co., Ltd. This study is funded by a Grant-in-Aid for JSPS Research Fellows No. 25•2388.

References

- Bauer D, Chaves H, Arcoumanis C (2012) Measurements of void fraction distribution in cavitating pipe flow using X-ray CT. *Meas Sci Technol* 23:055302. doi:[10.1088/0957-0233/23/5/055302](https://doi.org/10.1088/0957-0233/23/5/055302)
- Birkhofer BH, Jeelani SAK, Windhab EJ, Ouriev B, Linsner KJ, Braun P, Zeng Y (2008) Monitoring of fat crystallization process using UVP-PD technique. *Flow Meas Instrum* 19:163–169. doi:[10.1016/j.flowmeasinst.2007.08.008](https://doi.org/10.1016/j.flowmeasinst.2007.08.008)
- Geiger AB, Tsukada A, Lehmann E, Vontobel P, Wokaun A, Scherer GG (2002) In situ investigation of two-phase flow patterns in flow fields of PEFC's using neutron radiography. *Fuel Cells* 2:92–98
- Kotze R, Wiklund J, Haldenwang R (2012) Optimization of the UVP plus PD rheometric method for flow behavior monitoring of industrial fluid suspensions. *Appl Rheol* 22:42760. doi:[10.3933/AplRheol-22-42760](https://doi.org/10.3933/AplRheol-22-42760)

- Lee SJ, Kim GB, Yim DH, Jung SY (2009) Development of a compact X-ray particle image velocimetry for measuring opaque flows. *Rev Sci Instrum* 80:033706. doi:[10.1063/1.3103644](https://doi.org/10.1063/1.3103644)
- Murai Y, Tasaka Y, Nambu Y, Takeda Y, Gonzalez SR (2010) Ultrasonic detection of moving interfaces in gas–liquid two-phase flow. *Flow Meas Instrum* 21:356–366. doi:[10.1016/j.flowmeasinst.2010.03.007](https://doi.org/10.1016/j.flowmeasinst.2010.03.007)
- Ouriev B, Windhab EJ (2002) Rheological study of concentrated suspensions in pressure-driven shear flow using a novel in-line ultrasound Doppler method. *Exp Fluids* 32:204–211. doi:[10.1007/s003480100345](https://doi.org/10.1007/s003480100345)
- Sinton SW, Chow AW, Iwamiya JH (1994) NMR imaging as a new tool for rheology. *Macromol Symposia* 86:299–309. doi:[10.1002/masy.19940860123](https://doi.org/10.1002/masy.19940860123)
- Takeda Y (ed) (2012) *Ultrasonic Doppler velocity profiler for fluid flow*. Springer, Tokyo
- Wiklund J, Standing M (2008) Application of in-line ultrasound Doppler-based UVP-PD rheometry method to concentrated model and industrial suspensions. *Flow Meas Instrum* 19:171–179. doi:[10.1016/j.flowmeasinst.2007.11.002](https://doi.org/10.1016/j.flowmeasinst.2007.11.002)
- Wiklund J, Standing M, Trägårdh C (2010) Monitoring liquid displacement of model and industrial fluids in pipes by in-line ultrasonic rheometry. *J Food Eng* 99:330–337. doi:[10.1016/j.jfoodeng.2010.03.011](https://doi.org/10.1016/j.jfoodeng.2010.03.011)
- Wiklund J, Standing M, Pettersson AJ, Rasmuson A (2006) A comparative study of UVP and LDA Techniques for pulp suspensions in pipe flow. *AIChE J* 52:484–495. doi:[10.1002/aic.10653](https://doi.org/10.1002/aic.10653)
- Yanagisawa T, Yamagishi Y, Hamano Y, Tasaka Y, Yano K, Takahashi J, Takeda Y (2010) Detailed investigation of thermal convection in a liquid metal under a horizontal magnetic field. *Phys Rev E* 82:056306. doi:[10.1103/PhysRevE.82.056306](https://doi.org/10.1103/PhysRevE.82.056306)
- Zheng H, Liu L, Williams L, Hertzberg JR, Lanning C, Shandas R (2006) Real time multicomponent echo particle image velocimetry technique for opaque flow imaging. *Appl Phys Lett* 88:261915. doi:[10.1063/1.2216875](https://doi.org/10.1063/1.2216875)